

# Compact Mid-Infrared Chalcogenide Glass Photonic Devices Based on Robust-Inverse Design

Xiaobin Lin, Maoliang Wei, Kunhao Lei, Songtao Yang, Hui Ma, Chuyu Zhong, Ye Luo, Da Li, Junying Li, Changgui Lin, Wei Zhang, Shixun Dai, Xiaoyong Hu, Lan Li, Erping Li,\* and Hongtao Lin\*

Mid-infrared (mid-IR) on-chip photonic devices have attracted increasing attention because of their potential applications in chemical and biological sensing and optical communications. In particular, chalcogenide glasses (ChGs) have long been regarded as promising materials for mid-IR integrated photonics, owing to their broad infrared transparency, high nonlinearity, and excellent processing capabilities. Here, an inverse design approach is introduced to ChG photonic device design with a new robust inverse design method. A high-performance mid-IR inverse design polarization beam splitter, waveguide polarizer, mode converter, and wavelength demultiplexer are demonstrated for the first time. They all have a footprint of only several micrometers. The robust inverse design method could improve the robustness of device performance against fabrication variations and would be a general approach for designing and optimizing miniaturized chalcogenide photonic devices.

role in analytical science,<sup>[1,2]</sup> infrared imaging,<sup>[1]</sup> and optical communications.<sup>[1,3,4]</sup> Integrated photonic devices provide subwavelength-scale optical confinement to remarkably enhance light-matter interactions and have motivated great research enthusiasm. Several mid-IR integrated material platforms are currently developing, including suspended silicon,<sup>[5]</sup> germanium on silicon,<sup>[6]</sup> silicon on sapphire,<sup>[7]</sup> chalcogenide glasses (ChGs),<sup>[1,8,9]</sup> halide glasses,<sup>[10]</sup> etc. Particularly, ChGs have been regarded as promising materials for mid-IR integrated photonics owing to their excellent optical transparency (0.5–25.0  $\mu\text{m}$ ),<sup>[4]</sup> extremely high nonlinearity ( $(2\text{--}20) \times 10^{-18} \text{ m}^2 \text{ W}^{-1}$ ),<sup>[11]</sup> and substrate-blind integration capability.<sup>[8]</sup>

However, low-loss waveguides and microcavities based on ChGs can be directly fabricated on silicon or mid-IR transparent material substrates<sup>[12–14]</sup> for mid-IR sensing<sup>[1,15]</sup> and supercontinuum generation applications.<sup>[9,16–18]</sup> On the other hand, ChGs can also be integrated with novel optoelectronic materials such as 2D materials or III–V materi-

## 1. Introduction

The mid-infrared (mid-IR, 2–20  $\mu\text{m}$ ) band, which covers the primary absorption bands of most essential molecules and contains multiple atmospheric windows, plays a vital

X. Lin, M. Wei, K. Lei, S. Yang, H. Ma, C. Zhong, D. Li, J. Li, E. Li, H. Lin  
State Key Laboratory of Modern Optical Instrumentation  
College of Information Science and Electronic Engineering  
Zhejiang University  
Hangzhou 310027, China  
E-mail: liep@zju.edu.cn; hometown@zju.edu.cn

X. Lin, M. Wei, K. Lei, S. Yang, H. Ma, C. Zhong, D. Li, J. Li, E. Li, H. Lin  
Key Laboratory of Micro-Nano Electronics and Smart System of Zhejiang Province  
College of Information Science and Electronic Engineering  
Zhejiang University  
Hangzhou 310027, China


Y. Luo, L. Li  
Key Laboratory of 3D Micro/Nano Fabrication and Characterization of Zhejiang Province  
School of Engineering  
Westlake University  
Hangzhou 310024, China

Y. Luo, L. Li  
Institute of Advanced Technology  
Westlake Institute for Advanced Study  
Hangzhou 310024, China

C. Lin, W. Zhang, S. Dai  
Laboratory of Infrared Materials and Devices  
Ningbo University  
Ningbo 315211, China

X. Hu  
State Key Laboratory for Mesoscopic Physics  
Frontiers Science Center for Nano-optoelectronics  
School of Physics  
Peking University  
Beijing 100871, China

H. Lin  
MOE Frontier Science Center for Brain Science & Brain-Machine Integration  
Zhejiang University  
Hangzhou 310027, China

 The ORCID identification number(s) for the author(s) of this article can be found under <https://doi.org/10.1002/lpor.202200445>

DOI: 10.1002/lpor.202200445

als to develop active devices, including mid-IR modulators,<sup>[8,19]</sup> detectors,<sup>[8]</sup> and laser sources.<sup>[20,21]</sup> Moreover, ChGs with specific chemical compositions could exhibit nonvolatile phase transition characteristics, thus having great prospects for developing novel near-zero power reconfigurable devices.<sup>[22]</sup>

However, current ChG photonic devices still rely on standard photonic design libraries and mainly utilize regular-structure units. The traditional design approach, which is usually described by a small collection of tuning parameters, limits device performance, and size downscaling. As an efficient algorithm-assisted design method, inverse design has recently shown great potential in the design and optimization of photonic devices. Compared to traditional design methods, the inverse design approach is highly complementary to transformation optics and possesses higher design dimensions, which is beneficial for achieving devices with more complex functions and smaller footprints.<sup>[23]</sup> However, it also makes the device highly sensitive to manufacturing variations owing to its small feature size. Stochastic uncertainties, such as material composition fluctuations, geometry deviations, and processing errors, are inescapable and dramatically affect device performance. To date, inverse design has only been applied in constructing near-infrared (near-IR) wavelength demultiplexers,<sup>[24,25]</sup> mode converters (MCs),<sup>[26,27]</sup> computing structures,<sup>[28]</sup> and particle accelerators<sup>[29]</sup> based on silicon photonic platforms. Variations in manufacturing are an important factor hindering the progress of inverse-designed chalcogenide photonics.

In this study, we demonstrate compact mid-IR ChG photonic devices based on a robust inverse design method. A new robust inverse design method was developed to improve the device's performance against stochastic uncertainties related to manufacturing variations. For the first time, we experimentally demonstrated four mid-IR inverse-designed ChG photonic devices with small footprints: polarization beam splitter (PBS), waveguide polarizer (WP), MC, and wavelength demultiplexer. This study presents an effective use of the inverse design method and provides a technological pathway for future compact and high-performance mid-IR photonic architectures.

## 2. Results

### 2.1. Robust-Inverse Design

In recent years, the inverse design method has been widely used in nanophotonics,<sup>[23,24,27,30–32]</sup> in which evolutionary and gradient-based algorithms are two of the most commonly proposed optimization algorithms. For evolutionary algorithms, such as the genetic algorithm<sup>[33]</sup> and particle swarm algorithm,<sup>[34]</sup> optimization is driven by a neighborhood search. Because the algorithm is independent of the sensitivity between the objective and individual design parameters, it has a unique advantage in complicated non-convex objective functions. Nevertheless, for a similar number of design parameters, the computational cost of evolutionary algorithms is several orders of magnitude higher than that of gradient-based algorithms, and optimization is prone to the curse of dimensionality. The introduction of a gradient-based inverse design<sup>[35]</sup> can dramatically reduce computational costs. However, due to the high non-convexity of the optimization problem, the gradient-based

inverse design also faces the dilemma of a local optimum. In this study, we developed a new robust inverse method for the gradient-based algorithm in which weighted perturbations were introduced to break the local optimum and increase the robustness of the design without extra computing power.

For gradient-based inverse design, the optimization target is described as the minimization of the figure of merit (FOM) with respect to the design variables. Based on Maxwell's equations, the relationship between the FOM and the design parameter ( $\rho$ , material density) in electromagnetics is defined as:

$$\text{minimize}_{\rho} \text{FOM}(\rho) \quad (1a)$$

$$\text{subject to } \nabla \times \frac{1}{\mu} \nabla \times E - \omega^2 \mu \epsilon_0 \epsilon(\rho) E = -i\omega j \quad (1b)$$

$$0 \leq \rho \leq 1 \quad (1c)$$

where  $E$  represents the electric field,  $j$  is the current source,  $\mu$  is the magnetic permeability,  $\epsilon$  is the permittivity, and  $\rho$  is the material density that characterizes the device structure. As the first example, the structure of the inverse-designed PBS is shown in **Figure 1a**. The design area of the device was  $5 \times 5 \mu\text{m}^2$  and consisted of  $250 \times 250$  square cells on the horizontal plane. There are two possibilities for the material properties of each cell, where white indicates air ( $\rho = 0$ ) and black indicates the ChG material ( $\rho = 1$ ).

For the PBS, propagating light with different polarizations is split into different ports (TE/TM for output waveguide 1/2), and the FOM can be defined through the transmittance in different output waveguides as follows:

$$\text{FOM} = 1 - (T_{\text{out}_1\text{-TE}} + T_{\text{out}_2\text{-TM}}) \quad (2)$$

where  $T_{\text{out}_1\text{-TE}}$  and  $T_{\text{out}_2\text{-TM}}$  are the TE- and TM-mode transmittances of the selected output waveguides 1 and 2, respectively (refer Note S1, Supporting Information).

The new optimization process proceeded in three steps: Adjoint optimization, filtering and projection, and perturbation, as shown in **Figure 1b**. In the first step, the relative permittivity of the design area between air and ChG was continuous, and the gradient with respect to the material density was computed through adjoint sensitivity analysis. The objective function of the device quickly converges to the local optimum over iterations. In the second step, the three-field method<sup>[36]</sup> is used to transform the continuous material density into discrete values. By projecting the design field onto the physical field, we obtained an optimized physical structure without intermediate states in the area (refer Note S1, Supporting Information). Up to this point, the design only complied with physical constraints. However, there are still some unavoidable uncertainties in the fabrication processes, which could influence the performance and increase the model complexity. In the final step, we introduce perturbation into the optimization process and propose a new robust inverse optimization strategy.

$$\min_{\rho} \text{FOM}(\rho) = \begin{cases} \text{FOM}_0(\rho) & \beta \leq \beta_0 \\ \text{FOM}_0(\rho) + E_{\xi} \left[ (\text{FOM}^*(\rho, \xi) - \text{FOM}_0(\rho))^2 \right] & \beta > \beta_0 \end{cases} \quad (3)$$

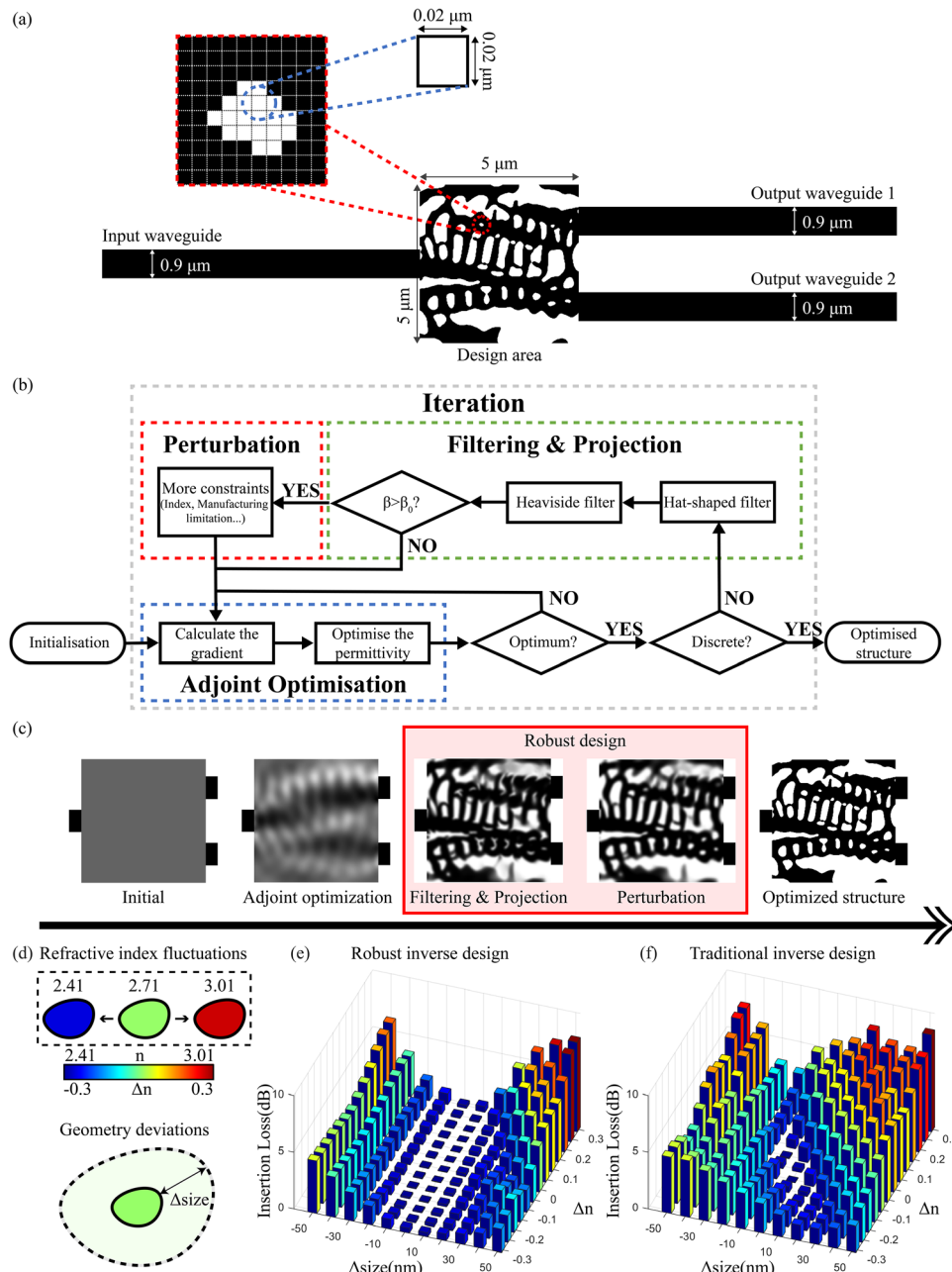


**Figure 1.** Schematic illustration of the design algorithm. a) Structure of the PBS constructed by inverse design method. The PBS consists of one input waveguide and two output waveguides with a width of  $0.9 \mu\text{m}$ . The  $5 \times 5 \mu\text{m}^2$  design region is connected between the waveguides and consists of cells with a size of  $0.02 \times 0.02 \mu\text{m}^2$ . b) The optimization procedure of the design algorithm, which contains adjoint optimization, filter and projection, and perturbation modules. c) The intermediate structures generated by the inverse design process. d) The fabrication variations introduced into the design. Insertion loss of the PBS with refractive index fluctuation and geometry deviation. e) robust-inverse design. f) traditional inverse design.

where  $\beta$  is the binarisation factor of the Heaviside filter in the three-field method and  $\beta_0$  is the threshold value.  $\xi$  is the vector describing fabrication variations, such as material composition fluctuations, geometry deviations, and processing errors. The  $FOM^*(\rho, \xi)$  is the target under perturbation, which describes the influence of manufacturing variations. During the fabrication process, the fabrication variations were randomly distributed and independent of each other. Given the probability density

function (PDF) of  $\xi$ , the expectation of the mean square error  $E_{\xi}[(FOM^*(\rho, \xi) - FOM(\rho))^2]$  was introduced to the objective function to improve the robustness of the design. Assuming that the PDF of the error was uniform, we could only calculate the device performance under maximum fabrication process variations. The intermediate structures generated by the optimization process are shown in Figure 1c. When the binarisation factor  $\beta$  in the Heaviside filter was greater than the set value,

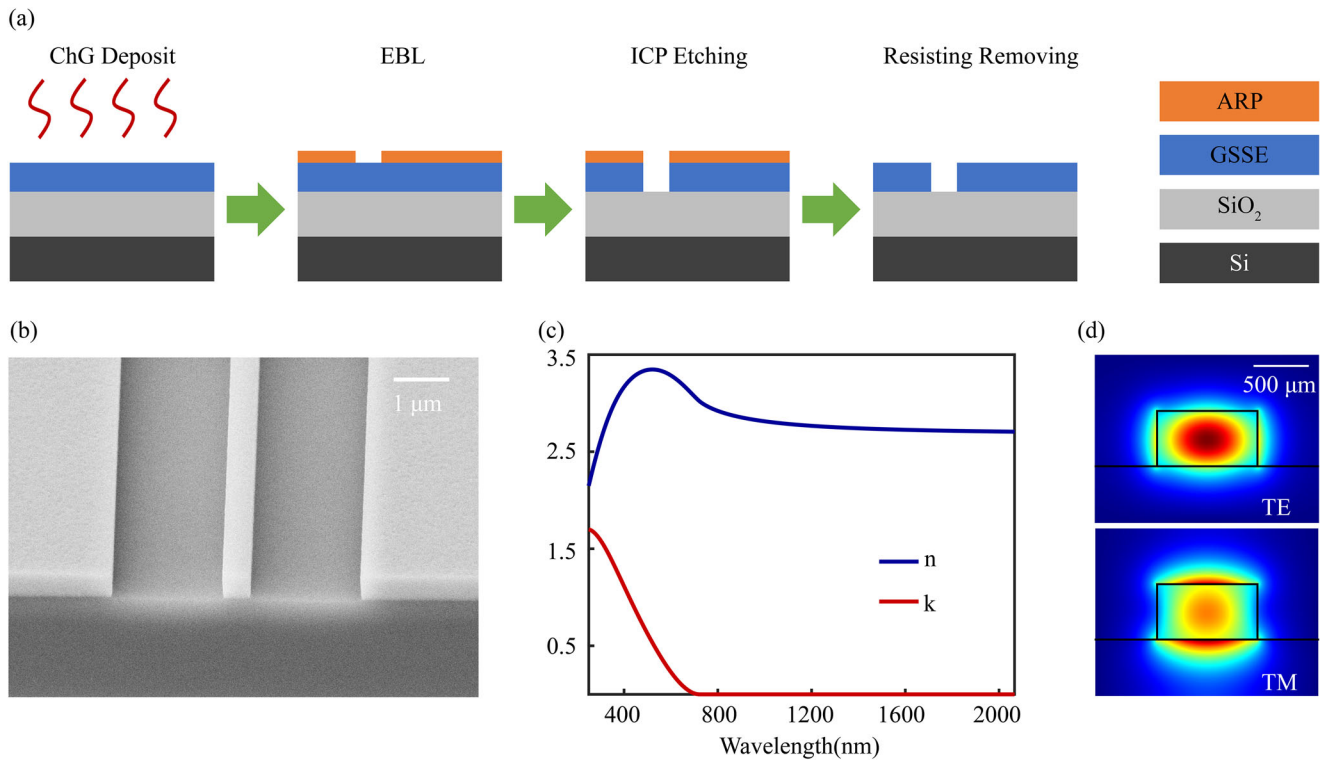


**Figure 2.** a) Schematic flow of ChG photonic device fabrication process. b) SEM image of the cross-section of the strip waveguide. c) Measured complex refractive index of ChG thin films. d) Simulated electrical field of the fundamental TE mode and TM mode in the strip waveguide.

new perturbations were inserted to increase the robustness of the device. The robustness of the device was increased while ensuring the performance of the device in almost the same optimization time. Using PBS as an example, we compared the traditional inverse design method with our robust inverse design method using a 2D simulation. Both methods took almost the same time and were computed in  $\approx 7$  h on a server with an Intel Xeon CPU E5-2620 processor and 128 GB RAM. As shown in Figure 1d–f, our robust-inverse design demonstrated a higher tolerance to refractive index fluctuation and geometry deviation than the traditional inverse method. The robust-designed device exhibited excellent performance ( $IL_{TE} + IL_{TM} < 1$  dB, @  $\approx 2025$ – $2075$  nm) under a range of  $\pm 20$  nm processing error and  $\pm 0.3$  refractive index deviation, which is almost ten times that of traditional designs (refer Note S2, Supporting Information).

## 2.2. Device Fabrication

The processing flow of the ChG device is shown in Figure 2a. The ChG film, which was composed of  $\text{Ge}_{28}\text{Sb}_{12}\text{Se}_{60}$  (GSSE), was deposited on top of a silicon substrate with 2 μm thick silicon oxide by thermal evaporation. The film was then exposed to  $100 \text{ mW cm}^{-2}$  UV light for 3 days and baked for an additional 3 h at  $150^\circ\text{C}$ .<sup>[37]</sup> Then, a positive-tone e-beam resist (ARP 6200.13) was spin-coated on the surface of the film, and the pattern was fabricated using electron beam lithography (Raith VOYAGER). Subsequently, the patterns were transferred to the ChG by inductively coupled plasma etching (Oxford Plasmapro100 Cobra 180),

followed by the removal of the e-beam resist. A scanning electron microscopy (SEM) image of the manufactured GSSE waveguide is shown in Figure 2b. As shown in Figure 2c, the material is almost lossless above the wavelength of 750 nm, and the refractive index is 2.71 around 2000 nm. To ensure that the mode energy of different polarization directions can be confined in the waveguide (Figure 2c), the rectangular waveguide was designed using Lumerical's eigenmode solver. The optimized single-mode waveguide size is  $0.9 \times 0.5 \mu\text{m}^2$ . The effective refractive index of TE<sub>0</sub> mode and TM<sub>0</sub> mode are 2.12 and 1.90 at 2025 nm, respectively.

## 2.3. PBS

As one of the key components in the integrated chip, the PBS can separate and combine different polarizations of light. As yet, various PBS photonic devices have been reported, such as multimode interferometers (MMI),<sup>[38]</sup> asymmetrical directional couplers (ADC)-based PBS,<sup>[39]</sup> and hetero-anisotropic metamaterials.<sup>[40]</sup> These traditional PBS devices achieve a high polarization extinction ratio (PER > 20 dB). However, they have disadvantages such as large device size ( $> 100 \mu\text{m}$ ), high insertion losses ( $IL > 2$  dB), and high sensitivity to phase matching. The near-IR silicon PBS optimized by the direct binary search (DBS) algorithm has realized an ultra-small size ( $2.4 \times 2.4 \mu\text{m}^2$ ),<sup>[31]</sup> but at the cost of time-consuming computing, a limited number of design variables, and reduced performance (PER < 10 dB) of the device.

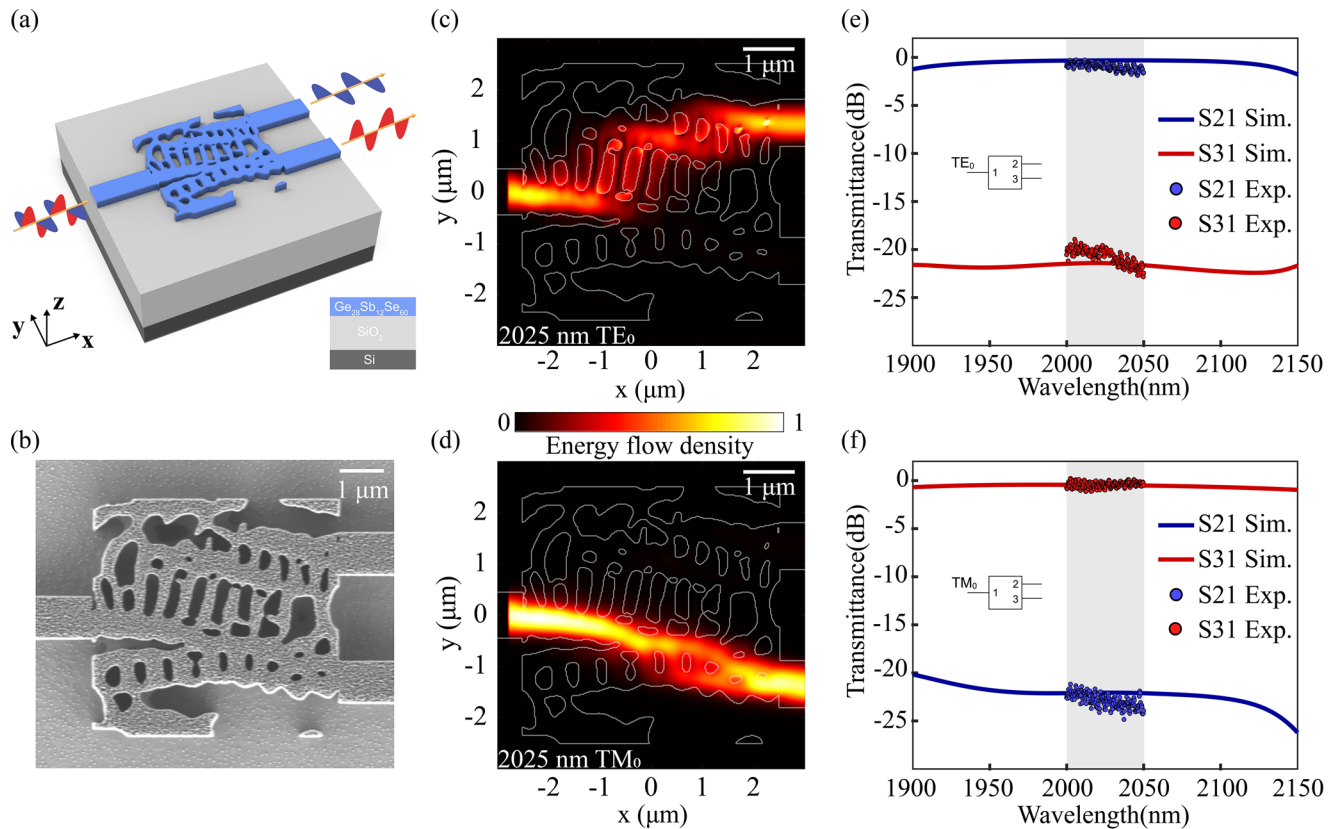


**Figure 3.** a) 3D view of the designed PBS. b) SEM image of the fabricated PBS. Simulated energy flow density plots of the device operating c) at TE mode and d) at TM mode. e) Transmission spectra of the devices operating at TE mode: the solid line represents simulation results, whereas the dots are experimental data. f) Transmission spectra of the devices operating at TM mode: the solid line represents simulation results, whereas the dots are experimental data.

Here, we used the algorithm described in Section 2 to design the device (refer the schematic diagram shown in **Figure 3a**). The SEM image of the device is shown in **Figure 3b**; it is composed of an input waveguide, two output waveguides, and a design area. **Figure 3c,d** shows the energy distribution of signals with different polarizations ( $TE_0$  and  $TM_0$ ) when the input wavelength was 2025 nm. When the  $TE_0$  light was sent into the input waveguide, multiple interferences occurred in the design area, the energy was mainly confined to the nanoholes in the area, and the slot waveguide effect was dominant. Conversely, for  $TM_0$  light, the energy was constrained primarily in the glass, and the GSSE film was used as the core layer to guide the light. The signal is directed opposite to the waveguide below.

To analyze the optimized design, we simulated the transmittance of the upper (blue line) and lower (red line) output waveguides under different polarization inputs with wavelengths ranging from 1900 to 2150 nm. As shown in **Figure 3e**, the maximum PER is 21.85 dB ( $TE_0$ , @2105 nm) and 28.98 dB ( $TM_0$ , @2150 nm), and the average IL of TE and TM modes are 0.55 dB and 0.56 dB. The bandwidth for the >20 dB extinction ratio was simulated to be 229 nm, whereas the IL was less than 1 dB (1906–2135 nm). **Figure 3f** shows the normalized experimental transmittance spectra. The device realized high polarization extinction ratio of  $PER_{TE} = 21.44 \pm 0.19$  dB (@2047 nm),  $PER_{TM} = 24.85 \pm 0.12$  dB (@2037 nm). The measured average IL was  $0.98 \pm$

0.04 dB (TE) and  $0.42 \pm 0.05$  dB (TM), and the bandwidth for the 20 dB extinction ratio was measured to be larger than 50 nm, limited by the operating bandwidth of the equipment. To the best of our knowledge, broadband (>50 nm) polarization beam splitting with a high extinction ratio ( $PER > 20$  dB) represents the performance record in the mid-IR band.

#### 2.4. WP

In addition to PBS, WP is an essential device that effectively reduces the polarization sensitivity of the device. The polarizer can eliminate the unwanted polarization of light while maintaining orthogonal polarization for low-loss transmission. Traditional on-chip polarizers, including narrow waveguides,<sup>[41]</sup> hybrid plasmonic polarizers,<sup>[42]</sup> and subwavelength gratings,<sup>[43]</sup> have disadvantages such as large size, large IL, and small working wavelength range. Here, we show a compact WP in the mid-IR band, which realizes a high broadband PER for different polarizations.

To realize the WP function, the FOM was defined according to the differences between the transmission of signals with different polarizations in the output waveguide. Similar to the previous optimization process, the working wavelength of the device was set to 2000 nm, and the FOM is described as follows:

$$FOM = 1 - (T_{out,TE} - T_{out,TM}) \quad (4)$$

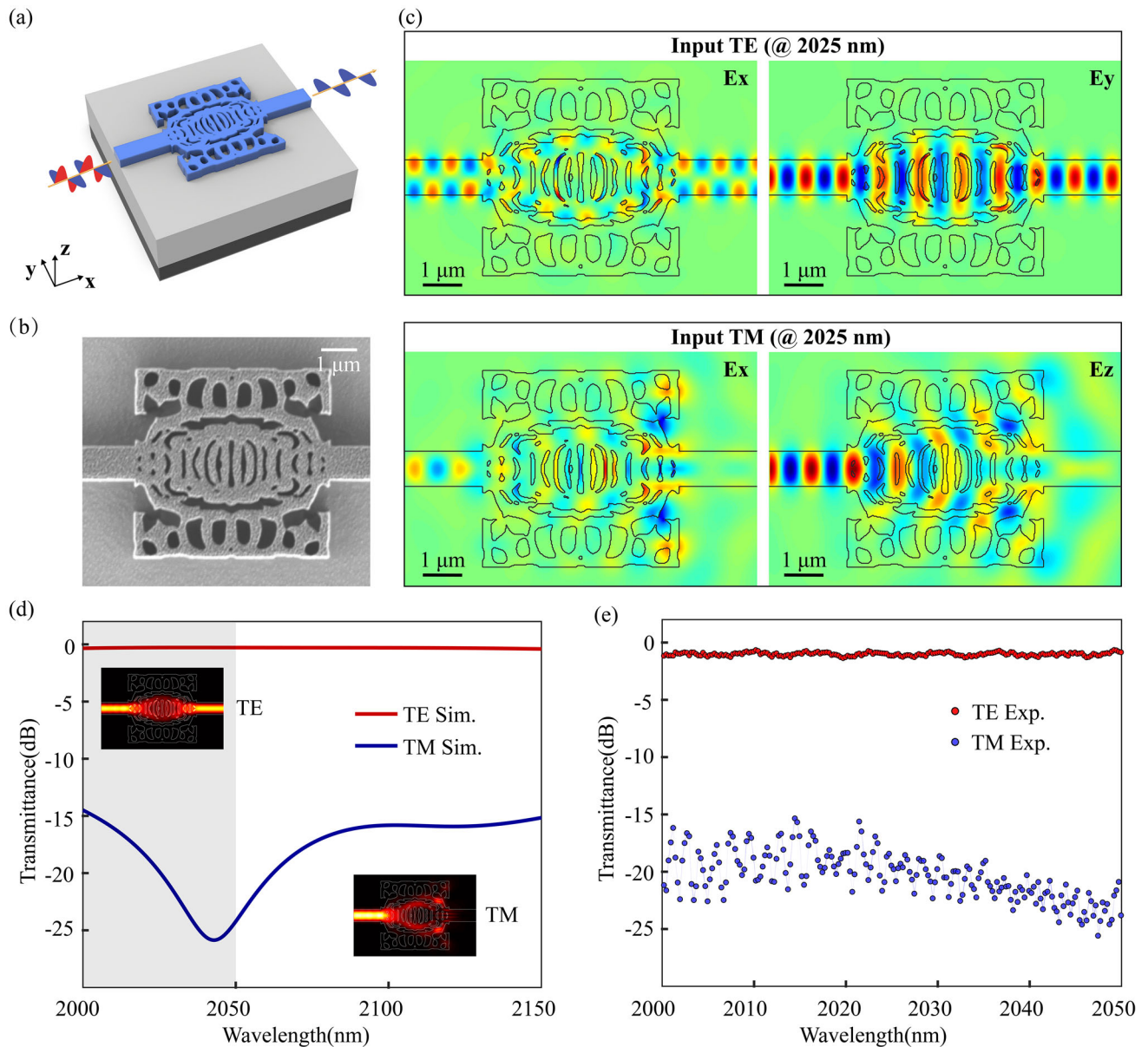


**Figure 4.** a) 3D view of the designed WP. b) SEM image of the fabricated WP. c) Simulated electric field plots of the device operating at TE and TM modes. d) Simulated transmission spectra of the devices operating at TE mode and TM mode (The insets are the energy flow density). e) Measured transmission spectra of the devices operating at TE mode and TM modes.

where  $T_{\text{out\_TE}}/T_{\text{out\_TM}}$  is the transmission of the TE/TM modes in the output waveguide.

A schematic diagram of the WP after optimization is shown in **Figure 4a**. To better analyze the working principle of the polarizer, the electric-field distribution of the device under different polarizations was simulated (**Figure 4c**). The robust inverse design algorithm generated nanocavities that were arranged nearly symmetrically along the central axis of the area. For the TE mode, the electric field was bound by the gaps, and the device functioned as a subwavelength waveguide to achieve efficient energy transmission. In contrast, for the TM mode, the nano-cavities in the center of the area effectively blocked the light, and the electric field spread around the device and could not be received by

the output waveguide. To further verify the bandwidth of the device, we calculated the transmission under different polarization from 2000 to 2150 nm, and the highest PER was calculated to be 25.86 dB (@ 2043 nm). As shown in **Figure 4d**, the bandwidth for <1 dB IL and >15 dB PER was  $\approx 147$  nm (2003–2150 nm). The SEM image of the fabricated device is shown in **Figure 4b**, and the experimental results are shown in **Figure 4e**. The device achieved a PER of 15 dB within a measured bandwidth of 50 nm while ensuring an IL of less than 1 dB. The same as the simulation, the maximum PER of  $24.43 \pm 0.09$  dB was measured at the wavelength of 2047 nm. To the best of our knowledge, this is the first demonstration of a high-performance inverse-designed WP with the smallest size at mid-IR.

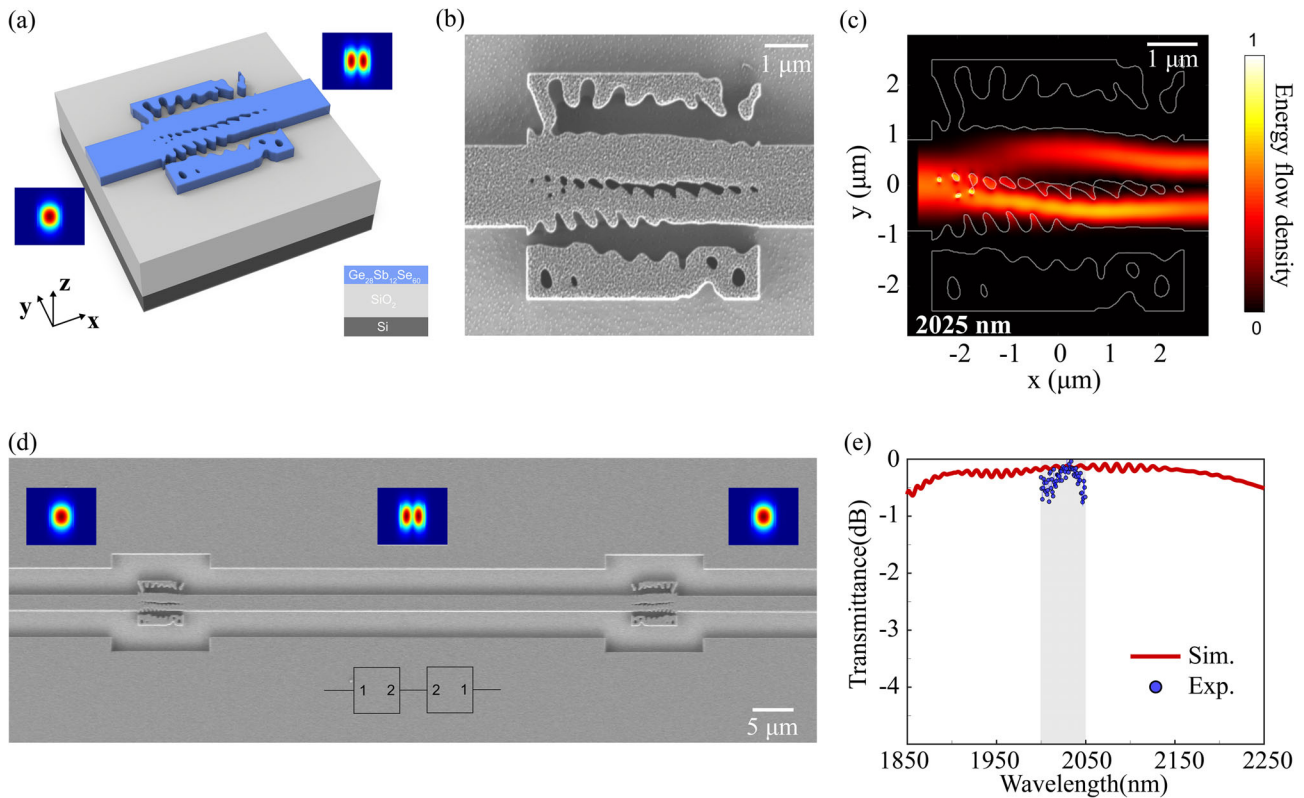


**Figure 5.** a) 3D view of the designed MC. b) SEM image of the fabricated MC. c) Simulated energy flow density plots of the device operating at 2025 nm. d) SEM image of the mode conversion system: the two devices are connected in reverse. e) Transmission spectrum of the mode conversion system: the solid line represents simulation results, whereas the dots are experimental data.

## 2.5. MC

MCs are the key building blocks of mode-division multiplexing (MDM) systems, which are capable of multiplexing different modes in the communication channel to dramatically increase the capacity of communication.<sup>[44]</sup> In this study, we present a mid-IR broadband MC device based on the same optimization algorithm. When the  $TE_0$  mode signal is ejected into the input port, it passes through the design area and is converted to the signal output of the  $TE_1$  mode.

To ensure that the waveguide can support both  $TE_0$  and  $TE_1$  modes, we increased the size of the waveguides to  $1.8 \times 0.5 \mu\text{m}^2$  and defined the FOM as the ratio between different modes:

$$\text{FOM} = 1 - \frac{T_{\text{out\_TE}_1}}{T_{\text{in\_TE}_0}} \quad (5)$$

where  $T_{\text{out\_TE}_1}$  is the transmission of the  $TE_1$  mode in the output waveguide and  $T_{\text{in\_TE}_0}$  is the transmission of the  $TE_0$  mode in the input waveguide.

**Figure 5a,b** shows the schematic and SEM images of the device, respectively. The algorithm creates a screen for air holes in the middle of the design area. When  $TE_0$  light was input into the device, the light was separated by the holes and outputted as  $TE_1$  light. In the experiment, we verified the performance by connecting the two devices in reverse, as shown in **Figure 5c**. By calculation, the bandwidth of the device after reverse connection

for IL of less than 1 dB was larger than 400 nm (1850–2250 nm), and the smallest IR was 0.08 dB (@2085 nm). The experimental test results showed that the average IL was  $0.39 \pm 0.05$  dB. Within a wavelength range of 50 nm, the IL of the device was less than 1 dB.

## 2.6. Wavelength Demultiplexer

In addition to MDM, wavelength division multiplexing (WDM) is also very important for mid-IR communication applications. Traditional WDM devices are primarily based on thin-film filters (TFF),<sup>[45]</sup> arrayed waveguide gratings (AWG),<sup>[46]</sup> microring resonators (MRR),<sup>[47]</sup> MMI,<sup>[48]</sup> and inverse design structures.<sup>[24,49]</sup> TFF is difficult for integrated circuits and has a large footprint, while it is difficult for the AWG to obtain a flat-topped response spectrum and a large wavelength spacing. MRR is sensitive to wavelength drift and has a narrow bandwidth. MMI requires multiple cascade structures to achieve good performance, and the device size is large.

For better device performance, the design area was extended to  $6 \times 6 \mu\text{m}^2$ , and the waveguide was  $0.5 \times 0.9 \mu\text{m}^2$ . The initial material refractive index was 2.71, and the relationship between the refractive index of the material and wavelength was also considered. The FOM was defined according to the transmission from the different output waveguides at different wavelengths. When signals with wavelengths of 1550 and 2025 nm were input, they

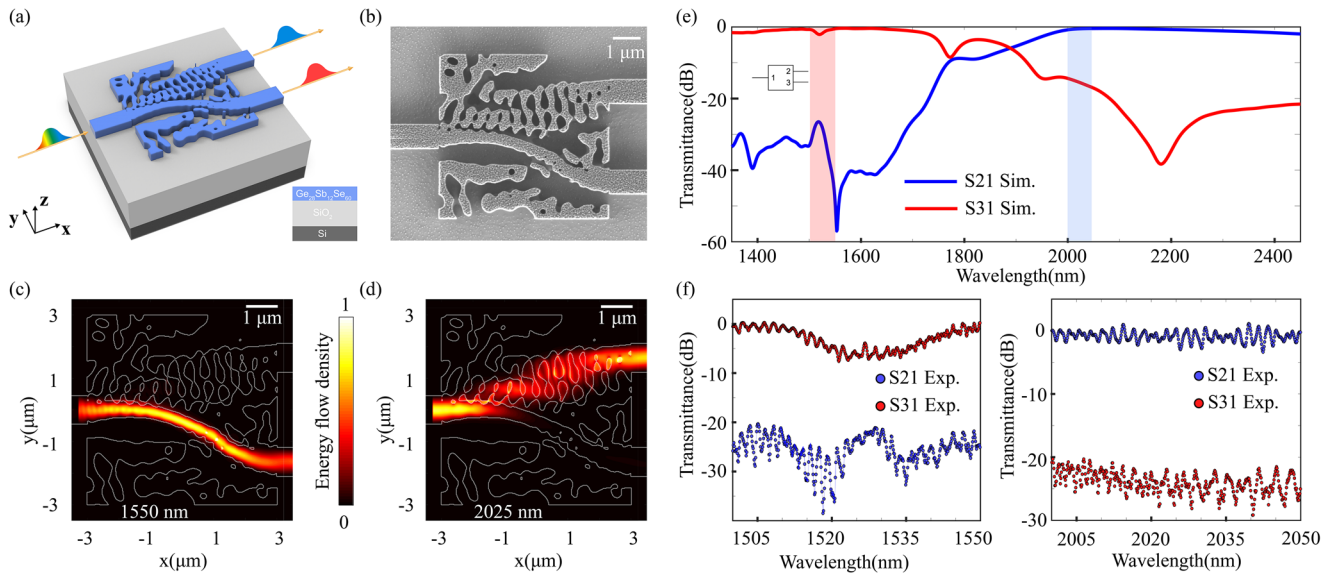


**Figure 6.** a) 3D view of the designed wavelength demultiplexer. b) SEM image of the fabricated wavelength demultiplexer. c) Simulated energy flow density plots of the device operating at 1550 nm. d) Simulated energy flow density plots of the device operating at 2025 nm. e) Simulated transmission spectra of the designed wavelength demultiplexer. Measured transmission spectra of the designed wavelength demultiplexer operating at f) 1500–1550 nm and g) 2000–2050 nm.

passed through the design area and were output separately from the up- and down-output waveguides, which construct the FOM function as follows:

$$\text{FOM} = \begin{cases} 1 - T_{\text{out\_down}}, & 1975 \text{ nm} \leq \lambda \leq 2075 \text{ nm} \\ 1 - T_{\text{out\_up}}, & 1400 \text{ nm} \leq \lambda \leq 1600 \text{ nm} \end{cases} \quad (6)$$

where  $T_{\text{out\_down}}/T_{\text{out\_up}}$  is the signal transmission in the down/up waveguide.

**Figure 6a** shows the structural diagram of the optimized WDM device under the same processing flow. An SEM image of the manufactured device is shown in **Figure 6b**. **Figure 6c,d** shows the energy distribution of the device at different wavelengths. When the wavelength of the input light was 2025 nm, energy was mainly transmitted in the nanocavity in the upper half of the design area. The air forms the core layer, and the light is finally output from the upper waveguide. In contrast, the light at 1550 nm was limited mainly to the ChG film and was transmitted into the output waveguide below. As shown in **Figure 6e**, the calculated results show that the extinction ratio (ER) of the device at 1550 nm was 48.25 dB within the IL of 0.38 dB and 16.86 dB within the IL of 0.42 dB at 2050 nm. The maximum ER is 56.55 dB (@1553 nm) and 37.66 dB (@2180 nm), which also achieved a flat-topped spectrum with a bandwidth greater than 374 nm at near-IR and 360 nm at mid-IR (ER > 20 dB). **Figure 6f** shows the experimental results. At 1550 nm, we got an ER of  $24.93 \pm 0.42$  dB, IL of  $0.83 \pm 0.14$  dB, and at 2050 nm, the ER reached  $24.65 \pm 0.05$  dB, IL of  $0.73 \pm 0.09$  dB.

### 3. Conclusion

In this study, we introduced the inverse design approach into ChG photonics and mid-IR photonics above a wavelength of 2 μm and demonstrated devices with four different complex

functions. For the PBS, the calculated bandwidth for the 20 dB  $\text{PER}_{\text{TE}}/\text{PER}_{\text{TM}}$  and 1 dB IL were  $\approx 262$  nm. The experimental results agreed well with the simulation of the device, achieving a high PER ( $\text{PER}_{\text{TE}} > 18$  dB,  $\text{PER}_{\text{TM}} > 20$  dB) and bandwidth of more than 50 nm (limited by laser equipment). For the WP, the simulation results showed the highest PER of 25.86 dB and the broad bandwidth of 147 nm, and the experimental results confirmed the broadband PER of 20 dB and the IL of less than 1 dB (2000–2050 nm). We also realized ultra-wideband MC devices (400 nm, IR > 1 dB) and experimentally demonstrated broadband mode conversion and low IL (50 nm, IR > 1 dB). Furthermore, a wavelength demultiplexer was designed to connect the near- and mid-IR regions. Simulation results showed that the broadband extinction ratio was achieved in both near-IR (ER > 20 dB, >374 nm) and mid-IR (ER > 20 dB, >360 nm), and the experimental results well verified the simulation results ( $24.93 \pm 0.42$  dB at 1550 nm,  $24.65 \pm 0.05$  dB at 2050 nm). We proposed a new topology optimization strategy, and the designs were extremely robust while ensuring performance with a small footprint. To the best of our knowledge, this is the first realization of these complex-functional ChG photonic devices in the mid-IR band. Moreover, this method can be adopted for more scenarios, such as refractive index perturbation optimization design, reconfigurable material optimization design, and nonlinear optimization design. It is possible to attract more research on nonlinear and reconfigurable inverse-designed chalcogenide photonic devices, which would inspire novel applications in all-optical processing and optical neural networks.

### 4. Experimental Section

**Measurement Methods:** The setup of the near-IR test system for the measurement of the wavelength demultiplexer is described in the previous works.<sup>[50]</sup> The mid-infrared test system was mainly composed of a



broadband tuning laser (Newfocus TLB-6700), a vertical fiber coupling platform, and a photodetector (PDA200C). The polarization direction of the light was controlled using a manual polarization controller and then fed into the chip. By scanning the wavelength of the laser, the output optical power of the device was detected by the photodetector, and the device transmission spectrum was measured.

## Supporting Information

Supporting Information is available from the Wiley Online Library or from the author.

## Acknowledgements

The research was partially supported by the National Natural Science Foundation of China (Grant numbers 91950204, 61975179, 62071424, 62027805, 62175202, and 92150302), the National Key Research and Development Program of China (2019YFB2203002), the Zhejiang Provincial Natural Science Foundation of China (LD22F040002, LD21F010002), the Leading Innovative and Entrepreneur Team Introduction Program of Zhejiang (2020R01005), the Open Fund of the State Key Laboratory of Integrated Optoelectronics (Grant number IOSKL2020KF05), the Fundamental Research Funds for the Central Universities (Grant number 2021QNA5007), and the Experimental Technology Research Program of Zhejiang University (Grant numbers SJS202010). The authors thank ZJU Micro-Nano Fabrication Center at Zhejiang University, Westlake Center for Micro/Nano Fabrication and Instrumentation, and Service Center for Physical Sciences at Westlake University for the facility support.

## Conflict of Interest

The authors declare no conflict of interest.

## Keywords

chalcogenide glass photonics, coherent optical communication, inverse design, mid-infrared

Received: June 18, 2022

Revised: October 11, 2022

Published online: December 18, 2022

- [1] B. J. Eggleton, B. Luther-Davies, K. Richardson, *Nat. Photonics* **2011**, 5, 141.
- [2] N. Singh, A. Casas-Bedoya, D. D. Hudson, A. Read, E. Mägi, B. J. Eggleton, *Opt. Lett.* **2016**, 41, 5776.
- [3] H. Lin, Z. Luo, T. Gu, L. C. Kimerling, K. Wada, A. Agarwal, J. Hu, *Nanophotonics* **2017**, 7, 393.
- [4] Y. Zhang, J. B. Chou, J. Li, H. Li, Q. Du, A. Yadav, S. Zhou, M. Y. Shalaginov, Z. Fang, H. Zhong, C. Roberts, P. Robinson, B. Bohlin, C. Rios, H. Lin, M. Kang, T. Gu, J. Warner, V. Liberman, K. Richardson, J. Hu, *Nat. Commun.* **2019**, 10, 4279.
- [5] Z. Zhang, G. I. Ng, T. Hu, H. Qiu, X. Guo, W. Wang, M. S. Rouifed, C. Liu, J. Sia, J. Zhou, C. G. Littlejohns, G. T. Reed, H. Wang, *IEEE Photonics J.* **2018**, 10, 6801608.
- [6] D. Marris-Morini, V. Vakarin, J. M. Ramirez, Q. Liu, A. Ballabio, J. Frigerio, M. Montesinos, C. Alonso-Ramos, X. Le Roux, S. Serna, D. Benedikovic, D. Chrastina, L. Vivien, G. Isella, *Nanophotonics* **2018**, 7, 1781.
- [7] A. Rostamian, J. Guo, S. Chakravarty, H. Yan, C. Chung, E. Heidari, R. T. Chen, *IEEE Photonics Technol. Lett.* **2019**, 31, 401.
- [8] H. Lin, Y. Song, Y. Huang, D. Kita, S. Deckoff-Jones, K. Wang, L. Li, J. Li, H. Zheng, Z. Luo, H. Wang, S. Novak, A. Yadav, C.-C. Huang, R.-J. Shiue, D. Englund, T. Gu, D. Hewak, K. Richardson, J. Kong, J. Hu, *Nat. Photonics* **2017**, 11, 798.
- [9] C. R. Petersen, U. Möller, I. Kubat, B. Zhou, S. Dupont, J. Ramsay, T. Benson, S. Sujecki, N. Abdel-Moneim, Z. Tang, D. Furniss, A. Seddon, O. Bang, *Nat. Photonics* **2014**, 8, 830.
- [10] S. Shalem, A. Katzir, *Opt. Lett.* **2005**, 30, 1929.
- [11] D. Duchesne, M. Ferrera, L. Razzari, R. Morandotti, B. E. Little, S. T. Chu, D. J. Moss, *Opt. Express* **2009**, 17, 1865.
- [12] P. Jean, A. Douaud, T. Thibault, S. LaRochelle, Y. Messaddeq, W. Shi, *Opt. Mater. Express* **2021**, 11, 913.
- [13] F. Wang, Z. Wang, D. Mao, M. Chen, Q. Li, T. Kananen, D. Fang, A. Soman, X. Hu, C. B. Arnold, T. Gu, *Adv. Opt. Mater.* **2020**, 8, 1901236.
- [14] C. K. Lai, D. Y. Choi, N. J. Athanasios, K. Yan, W. Y. Chong, S. Debbarma, H. Ahmad, B. J. Eggleton, M. Merklein, S. J. Madden, *Adv. Funct. Mater.* **2022**, 32, 2105230.
- [15] P. Su, Z. Han, D. Kita, P. Becla, H. Lin, S. Deckoff-Jones, K. Richardson, L. C. Kimerling, J. Hu, A. Agarwal, *Appl. Phys. Lett.* **2019**, 114, 051103.
- [16] Y. Yu, X. Gai, P. Ma, D. Choi, Z. Yang, R. Wang, S. Debbarma, S. J. Madden, B. Luther-Davies, *Laser Photonics Rev.* **2014**, 8, 792.
- [17] Y. Yu, X. Gai, T. Wang, P. Ma, R. Wang, Z. Yang, D. Choi, S. Madden, B. Luther-Davies, *Opt. Mater. Express* **2013**, 3, 1075.
- [18] J. Hwang, D. G. Kim, S. Han, D. Jeong, Y. H. Lee, D. Y. Choi, H. Lee, *Opt. Lett.* **2021**, 46, 2413.
- [19] L. Zhu, F. Liu, H. Lin, J. Hu, Z. Yu, X. Wang, S. Fan, *Light: Sci. Appl.* **2016**, 5, e16052.
- [20] Z. Li, Q. Du, C. Wang, J. Zou, T. Du, K. A. Richardson, Z. Cai, J. Hu, Z. Luo, *Laser Photonics Rev.* **2021**, 15, 2000301.
- [21] H. Lin, C. S. Kim, L. Li, M. Kim, W. W. Bewley, C. D. Merritt, C. L. Canedy, I. Vurgaftman, A. Agarwal, K. Richardson, J. Hu, J. R. Meyer, *Opt. Mater. Express* **2021**, 11, 2869.
- [22] C. Rios, M. Stegmaier, P. Hosseini, D. Wang, T. Scherer, C. D. Wright, H. Bhaskaran, W. H. P. Pernice, *Nat. Photonics* **2015**, 9, 725.
- [23] S. Molesky, Z. Lin, A. Y. Piggott, W. Jin, J. Vucković, A. W. Rodriguez, *Nat. Photonics* **2018**, 12, 659.
- [24] A. Y. Piggott, J. Lu, K. G. Lagoudakis, J. Petykiewicz, T. M. Babinec, J. Vučković, *Nat. Photonics* **2015**, 9, 374.
- [25] A. Y. Piggott, E. Y. Ma, L. Su, G. H. Ahn, N. V. Saprà, D. Verduyck, A. M. Netherton, A. S. P. Khope, J. E. Bowers, J. Vučković, *ACS Photonics* **2020**, 7, 569.
- [26] K. Wang, X. Ren, W. Chang, L. Lu, D. Liu, M. Zhang, *Photonics Res.* **2020**, 8, 528.
- [27] J. Lu, J. Vučković, *Opt. Express* **2013**, 21, 13351.
- [28] E. N. Mohammadi, B. Edwards, N. Engheta, *Science* **2019**, 363, 1333.
- [29] N. V. Saprà, K. Y. Yang, D. Verduyck, K. J. Leedle, D. S. Black, R. J. England, L. Su, R. Trivedi, Y. Miao, O. Solgaard, R. L. Byer, J. Vučković, *Science* **2020**, 367, 79.
- [30] J. S. Jensen, O. Sigmund, *Laser Photonics Rev.* **2011**, 5, 308.
- [31] B. Shen, P. Wang, R. Polson, R. Menon, *Nat. Photonics* **2015**, 9, 378.
- [32] H. Zhou, Y. Wang, X. Gao, D. Gao, J. Dong, D. Huang, F. Li, P. K. Alexander Wai, X. Zhang, *Laser Photonics Rev.* **2022**, 16, 2100521.
- [33] Z. Yu, H. Cui, X. Sun, *Photonics Res.* **2017**, 5, B15.
- [34] J. Robinson, Y. Rahmat-Samii, *IEEE Trans. Antennas Propag.* **2004**, 52, 397.
- [35] C. M. Lalau-Keraly, S. Bhargava, O. D. Miller, E. Yablonovitch, *Opt. Express* **2013**, 21, 21693.
- [36] M. Zhou, B. S. Lazarov, F. Wang, O. Sigmund, *Comput. Methods Appl. Mech. Eng.* **2015**, 293, 266.
- [37] S. Geiger, Q. Du, B. Huang, M. Y. Shalaginov, J. Michon, H. Lin, T. Gu, A. Yadav, K. A. Richardson, X. Jia, J. Hu, *Opt. Mater. Express* **2019**, 9, 2252.

- [38] Z. Wang, Y. Tang, L. Wosinski, S. He, *IEEE Photonics Technol. Lett.* **2010**, *22*, 1568.
- [39] C. Li, D. Dai, *Opt. Lett.* **2017**, *42*, 4243.
- [40] H. Xu, D. Dai, Y. Shi, *Laser Photonics Rev.* **2019**, *13*, 1800349.
- [41] W. Q. H. S., *IEEE Photonics J.* **2010**, *2*, 49.
- [42] M. Z. Alam, J. S. Aitchison, M. Mojahedi, *Opt. Lett.* **2012**, *37*, 55.
- [43] G. Quaranta, G. Basset, O. J. F. Martin, B. Gallinet, *Laser Photonics Rev.* **2018**, *12*, 1800017.
- [44] H. Jia, T. Zhou, X. Fu, J. Ding, L. Yang, *ACS Photonics* **2018**, *5*, 1833.
- [45] N. Yu, F. Capasso, *Nat. Mater.* **2014**, *13*, 139.
- [46] D. Dai, *J. Lightwave Technol.* **2017**, *35*, 572.
- [47] B. E. Little, S. T. Chu, J. V. Hryniewicz, P. P. Absil, *Opt. Lett.* **2000**, *25*, 344.
- [48] M. Rouifed, C. G. Littlejohns, G. X. Tina, H. Qiu, J. S. Penades, M. Nedeljkovic, Z. Zhang, C. Liu, D. J. Thomson, G. Z. Mashanovich, G. T. Reed, H. Wang, *Opt. Express* **2017**, *25*, 10893.
- [49] L. Su, A. Y. Piggott, N. V. Sapra, J. Petykiewicz, J. Vučković, *ACS Photonics* **2018**, *5*, 301.
- [50] J. Wu, M. Wei, J. Mu, H. Ma, C. Zhong, Y. Ye, C. Sun, B. Tang, L. Wang, J. Li, X. Xu, B. Liu, L. Li, H. Lin, *ACS Nano* **2021**, *15*, 15982.